RESEARCH ARTICLE

DOI: 10.54392/irjmt2657

INTERNATIONAL RESEARCH JOURNAL OF MULTIDISCIPLINARY TECHNOVATION

Asian Research Association

Tuning the Charge-Transport Properties of $CeTiO_3$ Thin Films through Controllable Phase Transformations Induced by the JNSP Technique

A. Yogeshwaran [a], A. Paramesvaran [b], R. Suresh [a, *]

[a] Department of Physics, Sri Ramakrishna Mission Vidyalaya College of Arts and Science, Coimbatore - 641 020, Tamil Nadu, India.

[b] Department of Physics, Sri Vasavi College, Erode - 638 316, Tamil Nadu, India.

* Corresponding Author Email: rsdphy@gmail.com

DOI: https://doi.org/10.54392/irjmt2657

Received: 16-06-2026; Revised: 15-08-2026; Accepted: 31-08-2026; Published: 11-09-2026

Abstract: $CeTiO_3$ thin films were synthesized by jet nebulizer spray pyrolysis (JNSP) at substrate temperatures of 350, 400, and 450 °C to investigate temperature-dependent structural, optical, morphological, and electrical properties for photodiode applications. X-ray diffraction analysis confirmed temperature-induced phase evolution and showed an increase in average crystallite size from 11.46 to 12.98 nm, accompanied by a reduction in dislocation density. FESEM observations revealed progressive grain growth and improved film densification, with average particle size increasing from approximately 17 to 35 nm. UV–Vis analysis demonstrated a decrease in optical band gap from 2.96 to 2.64 eV as the substrate temperature increased, indicating enhanced visible-light absorption. XPS confirmed the presence of Ce, Ti, and O with mixed Ce^{3+}/Ce^{4+} states and predominantly Ti^{4+}. $CeTiO_3$/p-Si photodiodes were fabricated and evaluated through current-voltage measurements under illumination. Device performance improved with increasing deposition temperature, with the 450 °C sample exhibiting the lowest ideality factor of 1.991, the highest barrier height of 0.411 eV, responsivity of 5.97 mA/W, quantum efficiency of 8.89%, and detectivity of 5.66 × 10^10 Jones. These results demonstrate that substrate-temperature control effectively tunes $CeTiO_3$ thin-film properties and enhances photodiode performance. The optimized films therefore show strong potential for oxide-based optoelectronic and photodetection device applications.

Keywords: Thin Films, $CeTiO_3$, JNSP, Electrical Characteristics, Photodiode, Optoelectronic Applications

1. Introduction

From the earliest spark of electronic discovery to the rapid pulse of today's technology, the P-N junction diode sits at the heart of countless innovations. This unassuming union of p-type and n-type semiconductors forms the backbone of modern electronics, where the dance between electrons and holes orchestrates current flow and blocks reverse signals. The depletion region, an invisible frontier, emerges at the interface, acting as both gatekeeper and catalyst for electronic action [1, 2]. When forward bias narrows this barrier, a surge of carriers transforms potential into performance, while a reverse bias stretches the region, stubbornly resisting current except for the faintest leakage [3].

Yet as electronic demands grow more sophisticated, the search for novel materials and architectures has led to remarkable breakthroughs. Among these, the $CeTiO_3$/p-Si junction diode stands out for its extraordinary properties and transformative applications. The adoption of cerium titanate, with its remarkable dielectric stability and tuneable band gap, marks a leap forward in diode engineering. Innovative fabrication, rooted in meticulous surface preparation and high-temperature annealing, optimizes interface quality, unlocking new levels of crystallinity and electrical performance [4, 5]. The resulting heterojunction, further enhanced by precision metal contacts, creates a device capable of thriving in the dynamic environments of optoelectronics and renewable energy systems. By combining advanced materials science with innovative engineering, the $CeTiO_3$/p-Si diode opens a new chapter in electronic device development, offering versatility and efficiency and previewing the future of integrated technology [6, 7].

In this unfolding narrative of advanced materials, this study examines the intricate interplay of structure, optics, and morphology in $CeTiO_3$ films, probing their potential to revolutionize PN junction diode technology. Our work centers on the innovative use of JNSP to fabricate $CeTiO_3$ layers, using precise control of deposition variables, precursor concentration,

sputtering time, and substrate temperature, to tailor film properties. Morphological and elemental analyses show how uniformity, chemical purity, and particle characteristics converge to shape device functionality at the microscopic level [8, 9]. Electrical analyses further decode the signature traits that govern diode behaviour, offering a window into the underlying mechanisms of performance. These findings identify $CeTiO_3$ as a strong candidate for next-generation optoelectronic applications, with device outcomes closely tied to fabrication distinctions and rigorous performance evaluation [10, 11].

2. Experimental Details

The synthesis of $CeTiO_3$ perovskite films was meticulously controlled by substrate temperatures of 350, 400, and 450 °C, each chosen to optimize crystalline quality and device performance. The fabrication process commenced with the rigorous preparation of fluorine-doped tin oxide (FTO) substrates, each measuring 2 cm by 1.5 cm. Substrates were first rinsed with deionized water to remove surface particulates, then immersed in a 0.1% Triton X-100 solution for 10-15 minutes to dislodge residual contaminants. Gentle mechanical cleaning using a lint-free cloth or soft-bristled brush further ensured pristine surfaces. Subsequent rinsing with deionized water effectively removed detergent traces, followed by sequential washes in isopropyl alcohol (5–10 minutes) and a final deionized water rinse to eradicate organic impurities. Table 1 lists the parameters used to deposit $CeTiO_3$ thin films by the JNSP technique.

For the precursor solution, dissolve 0.4 M cerium chloride ($CeCl_3 \cdot 7H_2O$) and titanium trichloride ($TiCl_3$, ≤12%) in 20 mL of double-distilled deionized water. The solutions were stirred individually for 2 hours at 300 rpm, then combined in equal volumes (10:10 mL) and agitated for an additional 2 hours to ensure homogeneity. After ultrasonic cleaning, the FTO substrates were thermally annealed at the target temperatures, completing the synthesis and promoting optimal film formation. Figure 1 summarizes the preparation workflow, capturing the systematic approach underpinning $CeTiO_3$ film development.

3.1 X-Ray Diffraction

X-ray diffraction (XRD) analysis of $CeTiO_3$ films deposited at different temperatures.

Table 1. Parameters utilized for the deposition of $CeTiO_3$ thin films through the JNSP technique

S.No	Parameters	Values
1.	Nozzle-to-substrate distance	5 cm
2.	Spray rate	0.5 ml/min
3.	Carrier-gas pressure	3.5 Kg/cm^2
4.	Total sprayed volume	15 ml
5.	Deposition duration	20 min
6.	Spray cycle	4
7.	substrate-temperature tolerance	±10

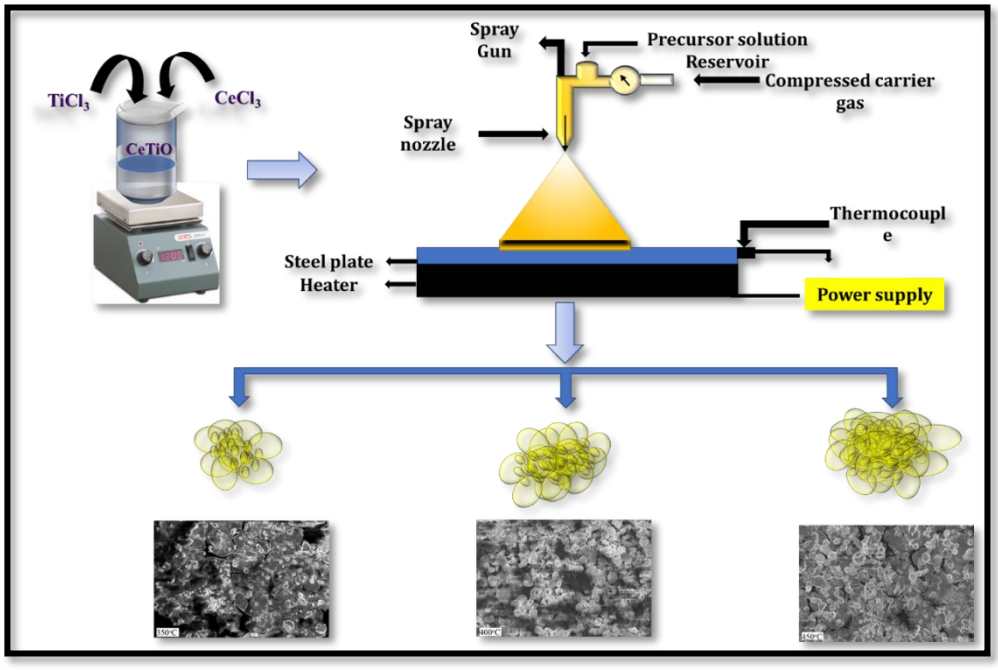

Figure 1. Schematic Representation of the Preparation of $CeTiO_3$ films.

Especially, the XRD patterns recorded for different 2θ values for the sample prepared at 350°C are The prominent diffraction peaks at angles θ = 29.21°, 33.83°, 38.36°,48.17°, 52.23°,56.94°, corresponding to the patterns (202), (212), (-113), (520), (114), and (132), are in good agreement with the $CeTiO_3$ thin film JCPDS card No.: 00–047-0667The angles θ = 29.21°, 33.83°,48.17°,56.94°, and 57.17°, corresponding to (111), (200), (220), (311), and (311), respectively, are found to be well matched with the CeO thin film JCPDS card No.: 00–001-0800. The angles θ = 56.94° and 57.17°, corresponding to the (131) indices, agree well with the TiO thin-film JCPDS card No.: 01–084-1750. The detected peaks correspond to the orthorhombic phase of TiO_2, the monoclinic phase of $CeTiO_3$, and the cubic phase of CeO, respectively. The results show that the diffraction peaks change significantly as temperature increases, shifting from a cubic structure to a monoclinic structure and then to an orthorhombic structure. These phase changes can be attributed to cerium, which affects crystallinity and weakens the preferred (111) direction. Although higher temperatures appear to reduce crystallinity in specific directions, improved grain size indicates increased crystallinity and fewer film boundaries [12]. This improvement reduces dispersion in the particle layer and minimizes contamination. The average crystallite size was determined by the Debye-Scherrer equation using the full width at half maximum (FWHM) of the XRD peaks. The diffraction patterns of all samples correlate well with the reference phase, indicating a consistent phase relationship among the samples. These observations demonstrate how temperature affects the structure and crystallinity of $CeTiO_3$ films. The XRD data shown in Figure 2 provide important information on the evolution and phase transitions of these films as a function of temperature.

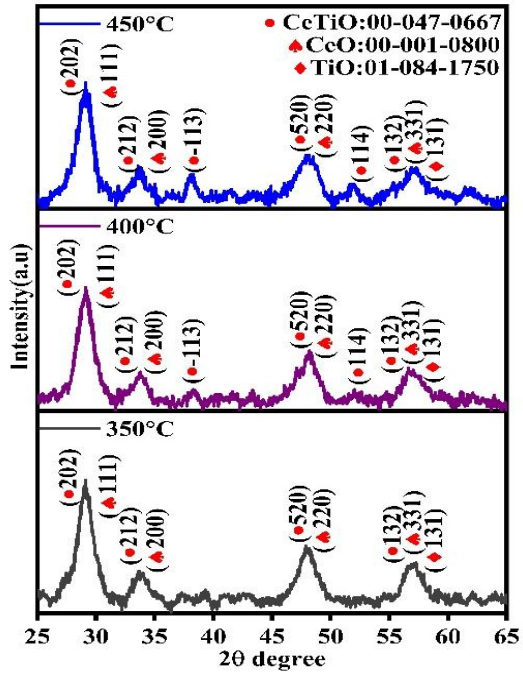

Figure 2. X-ray diffraction patterns of $CeTiO_3$ thin films at different temperatures.

$$D = \frac{k\lambda}{\beta \cos\theta} \quad (1)$$

Specific experiments determined the film properties, leading to calculations for crystallite size and measurements of strain (ε), dislocation velocity (δ), and stacking faults (SF).

The Debye-Scherrer formula determines crystallite size using k = 0.94, where α is the X-ray source wavelength, and β is the Bragg angle θ. In contrast, β represents the width of the half-maximum of the diffraction peak (FWHM). These measurements show how various factors interact to affect crystallinity and defect levels in $CeTiO_3$ films. Film coatings used in advanced applications require these evaluation measurements to assess their quality and performance characteristics.

$$\varepsilon = \beta \frac{\cos\theta}{4} \quad (2)$$

$$\delta = \frac{1}{D^2} \quad (3)$$

$$SF = \left[\frac{2\pi^2}{45(3\tan\theta)^{\frac{1}{2}}}\right]\beta \quad (4)$$

As temperature rises, $CeTiO_3$ lattice microstrain, dislocation density, and stacking faults emerge. The data reveal that each parameter, such as dislocation density, microstrain, and stacking fault value, increases as Ce content rises throughout the samples (Tables 2 & 3). The decrease in the diffraction-pattern peak is associated with increased absorption and increased crystallite size [13]. However, no prominent Ce peak was observed in the diffraction pattern, which could be temperature-dependent. The incorporation of Ce into the $CeTiO_3$ lattice destroys the crystal structure of $CeTiO_3$ and leads to a decrease in crystallinity. Reducing grain size can improve grain growth in the crystal lattice, affecting the lattice parameters of $CeTiO_3$ films [14]. XRD analysis shows that this structural change makes the material very suitable for optoelectronic applications. As the crystal grows, grain formation increases lattice uniformity, which is essential for optimizing thin films in electronic and photonic devices. These findings show that Ce not only affects the structure of $CeTiO_3$ but also tunes its bulk properties, supporting better optoelectronic integration. The structure obtained from this analysis shows that controlled temperature and lattice modifications can enhance material performance and pave the way for use in advanced optoelectronic applications [15].

3.2 FT-IR Analysis

Spectroscopic analysis (Figure 3) revealed distinct absorption bands, with prominent features at 2338.83 cm^{-1}, 1778.59 cm^{-1}, and below 700 cm^{-1}, alongside weaker bands spanning 1159.99-882.17 cm^{-1} and at 1673.67 cm^{-1}.

Table 2. Calculated structural parameters for $CeTiO_3$ thin films

Temp °C	2 theta	FWHM	Cry Size. (nm)	Dis. Density	Strain	Staking fault	hkl	Cry. Structure
350	29.21	0.39	20.9	2.29	0.17	0.028	202	Monoclinic
							111	Cubic
	33.83	1.10	7.5	17.61	0.13	0.085	212	Monoclinic
							200	Cubic
	48.17	1.10	7.8	16.03	0.15	0.101	520	Monoclinic
							220	Cubic
	56.94	0.94	9.5	10.92	0.16	0.094	132	Monoclinic
							311	Cubic
							131	Orthorhombic
400	29.10	1.41	5.7	29.80	0.10	0.101	202	Monoclinic
							111	Cubic
	33.68	0.47	17.5	3.23	0.17	0.036	212	Monoclinic
							200	Cubic
	38.36	0.47	17.8	3.15	0.17	0.038	-113	Monoclinic
	48.16	0.78	11.1	8.18	0.16	0.072	520	Monoclinic
							220	Cubic
	52.23	0.55	16.1	3.87	0.18	0.052	114	Monoclinic
	57.17	0.94	9.6	10.90	0.16	0.094	311	Cubic
							131	Orthorhombic
450	29.10	1.41	5.8	29.80	0.10	0.101	202	Monoclinic
							111	Cubic
	33.68	0.47	17.6	3.23	0.17	0.036	212	Monoclinic
							200	Cubic
	38.36	0.47	17.8	3.15	0.17	0.038	-113	Monoclinic
	48.16	0.78	11.1	8.18	0.16	0.072	520	Monoclinic
							220	Cubic
	52.23	0.55	16.1	3.87	0.18	0.052	114	Monoclinic
	57.17	0.94	9.6	10.90	0.16	0.094	311	Cubic
							131	Orthorhombic

Table 3. Average Structural parameters of spray-coated $CeTiO_3$ thin films

Temp (°C)	Crystalline Size D(nm)	Dislocation density (δ) $\times 10^{-14}$ (lines cm^{-2})	Micro Strain (ε)	Staking fault (SF) $\times 10^{-2}$
350	11.46	7.6091	0.1636	0.0729
400	12.33	6.5794	0.1621	0.0773
450	12.98	5.9377	0.1592	0.0661

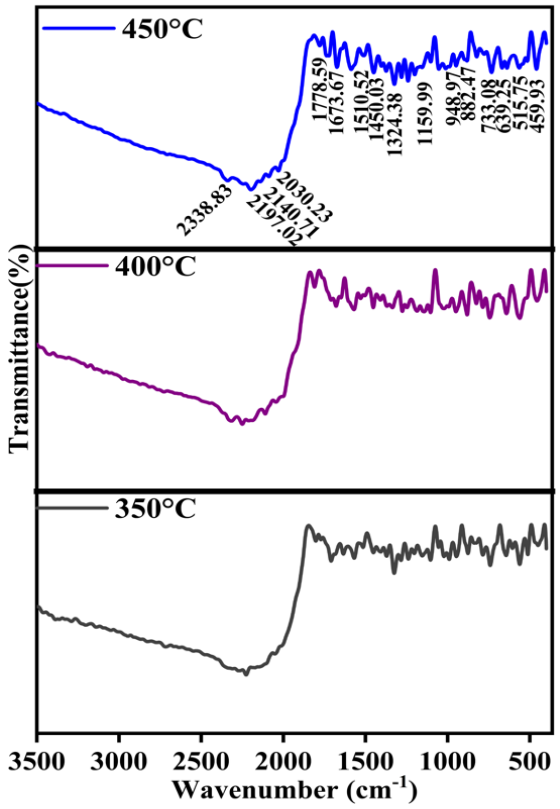

Figure 3. FT-IR spectra of $CeTiO_3$ thin films at different temperatures.

These vibrational signatures correspond to different molecular motions within the material. The broad absorption region between 2338.83 and 2030.23 cm^{-1}, notably associated with carbon–carbon triple-bond (C≡C) stretching, indicates the presence of alkyne groups. In contrast, the less intense bands observed from 1778.59 to 1159.99 cm^{-1} can be attributed to the stretching vibrations of carbonyl (C=O) functional groups in organic compounds, followed by in-plane bending modes of hydroxyl (O–H) functionalities. Additional absorptions between 960 and 850 cm^{-1} suggest residual organic or carbonate-like species adhered to the cerium surface [16]. The dominant absorption at approximately 700 cm^{-1} is characteristic of the phonon vibration envelope of the cerium oxide (CeO) lattice network. This comprehensive spectral profile elucidates the material's chemical structure, highlighting organic functionalities and the intrinsic framework of CeO_2. Collectively, these vibrational features offer insights into the composition and morphology of the examined samples, illuminating the interactions between organic residues and metallic constituents [17, 18].

3.3 FESEM and EDX Analysis

Scanning electron microscopy reveals that the surface morphology of $CeTiO_3$ thin films depends strongly on substrate temperature, with clear transitions in particle size, packing density, and defect structure.

At the lowest substrate temperature (350°C, Figure 4(a)), the films contain small, spherical particles averaging about 17 nm in diameter. The particle distribution is relatively loose, and the film surface displays visible cracks and discontinuities. These features suggest limited atomic mobility during deposition, resulting in incomplete grain coalescence and a high density of interparticle voids. This microstructure is typically associated with increased surface roughness, higher defect density, and suboptimal crystallinity [19].

As the substrate temperature increases to 400°C (Figure 4(b)), the films undergo a notable morphological transformation. The spherical particle size increases to about 26 nm, and the grains pack more closely, although some open boundaries and small voids persist. The improved packing density reflects enhanced surface diffusion and atomic rearrangement, which promote grain growth and interconnection. The reduction in cracks and voids, compared with the lower-temperature sample, indicates the onset of more robust film formation and improved structural integrity.

At the highest substrate temperature examined (450°C, Figure 4(c)), the SEM images reveal a highly dense nanostructured morphology composed of well-defined spherical balls averaging 34 nm in diameter. The particles are tightly packed, forming a continuous and cohesive film with minimal visible defects or surface irregularities. This dense arrangement indicates optimal grain growth and film densification, driven by sufficient thermal energy to enable extensive atomic migration and grain-boundary healing.

Overall, the SEM analysis confirms that higher substrate temperatures significantly improve microstructural quality, including larger grain size, enhanced packing density, and reduced surface defects [20]. These morphological advancements are expected to directly contribute to superior electronic transport and optoelectronic performance in $CeTiO_3$-based devices.

Examining the elemental composition of $CeTiO_3$ films, electron diffraction spectroscopy (EDX) revealed near-perfect stoichiometry and remarkable chemical uniformity (Figure 5). Each elemental signature titanium (Ti), cerium (Ce), and oxygen (O), emerged in harmony, echoing the theoretical composition of $CeTiO_3$ and underscoring the precision of the deposition process (Table 4). By systematically varying deposition temperatures, researchers gained new insights into the delicate balance of stoichiometry and homogeneity, revealing the robust stability of base-ratio compositions across experimental conditions [21]. The pronounced EDX peaks for Ce, Ti, and O, coupled with minimal impurity traces, attest not only to the film's high purity but also to the sophistication of the synthesis technique.

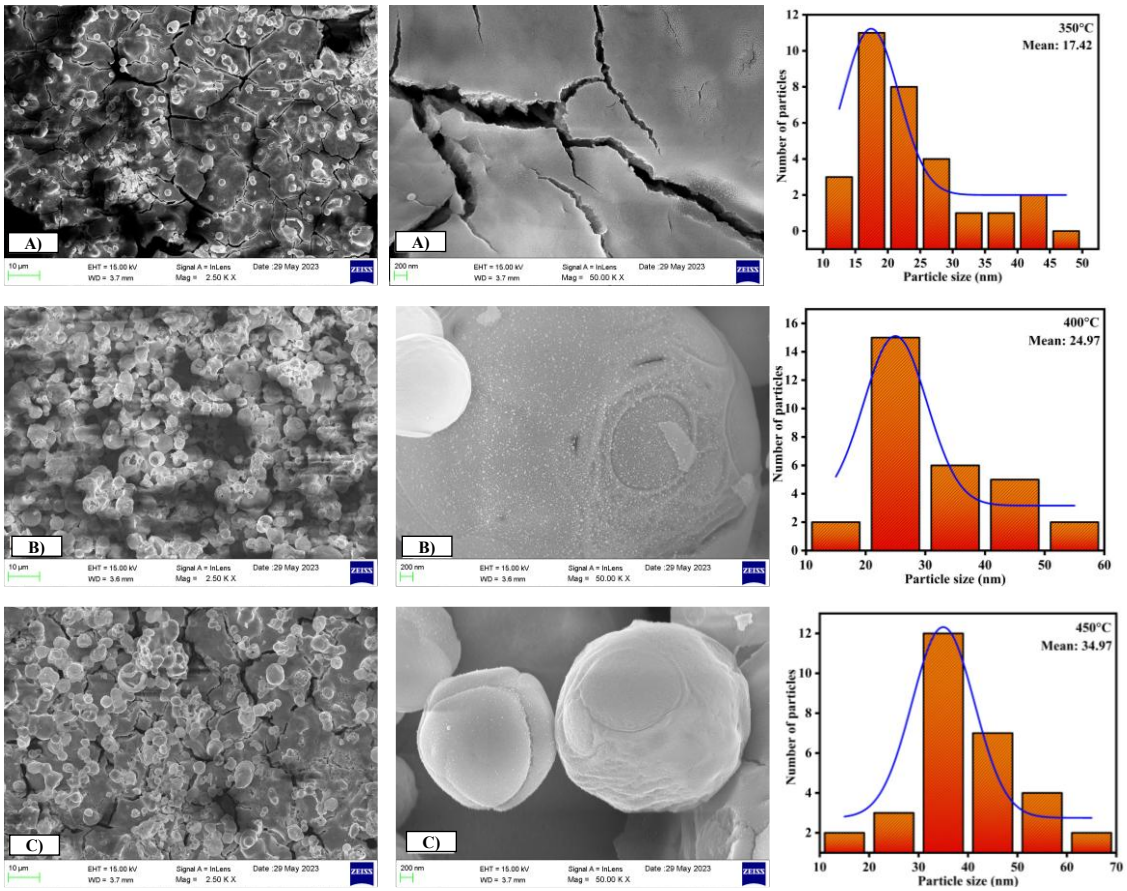

Figure 4 (a-c). FESEM images of $CeTiO_3$ thin films at different temperatures.

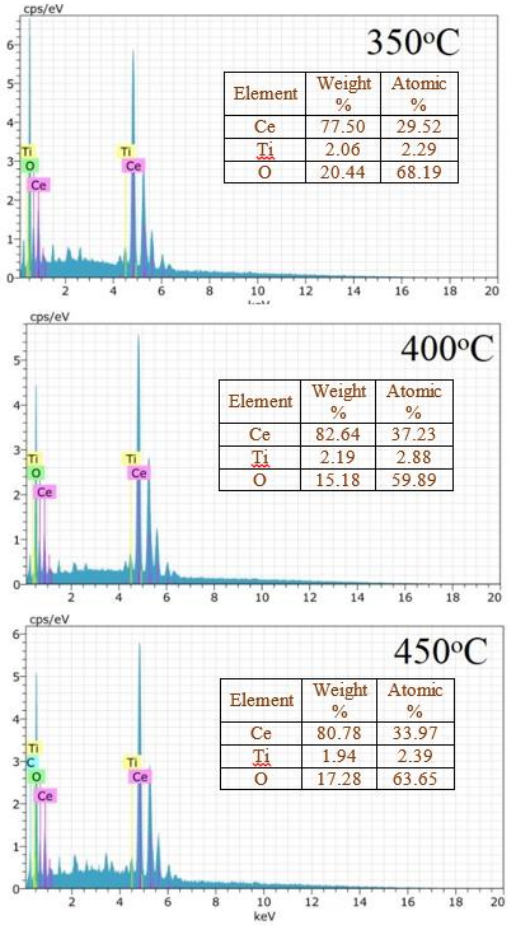

Figure 5. EDAX Spectra of $CeTiO_3$ thin films at different temperatures.

Table 4. The measured atomic percentages of Ce, Ti, and O

Deposition temperature	Ce(at.%)	Ti(at.%)	O(at.%)
350°C	29.52	2.29	68.19
400°C	37.23	2.88	59.89
450°C	33.97	2.39	63.65

3.4 XPS Analysis

Figure 6 shows the XPS Spectra of the sprayed $CeTiO_3$ thin film. Spectrum analysis confirmed the presence of various oxidation states of Ce 3d, Ce 4d, Ce 4p, Ti 2p, and O1s in the prepared films, providing a better understanding of the chemical composition (Table 5). Figure 6(a) presents the full survey XPS spectrum of $CeTiO_3$ films, delineating the elemental composition across the sample surface. The spectrum shows distinct peaks for Ce, Ti, and O, confirming successful incorporation of these elements into the perovskite matrix [22]. The absence of significant extraneous peaks attests to the material's high purity and the deposition process's effectiveness in minimizing surface contamination. The relative peak intensities allow an initial estimate of atomic ratios, which are consistent with the expected stoichiometry of $CeTiO_3$, establishing a foundation for further high-resolution analysis. Figure 6(b) shows the high-resolution Ce 3d XPS spectrum, characterized by a complex multiplet structure. The deconvolution of the Ce 3d peaks reveals the coexistence of Ce^{3+} and Ce^{4+} oxidation states [23]. These mixed-valence species are critical because they directly influence the film's electronic structure and potential catalytic activity. The relative abundance of Ce^{3+} to Ce^{4+} provides insight into the material's redox flexibility, which may enhance charge transport and promote defect-mediated functionalities in device applications. Figure. 6(d) focuses on the Ti 2p core-level spectrum. The peaks observed at binding energies characteristic of Ti^{4+} indicate that titanium is predominantly present in its fully oxidized state. The sharpness and symmetry of the Ti $2p_{3/2}$ and Ti $2p_{1/2}$ peaks suggest a well-ordered local environment around titanium atoms, signifying successful incorporation into the perovskite lattice without significant distortion or reduction [24]. This result is vital for ensuring robust electronic properties and phase stability in the $CeTiO_3$ films. Fig. 6(e) shows the O 1s XPS spectrum, which reveals two main components: a lower-binding-energy peak attributable to lattice oxygen and a higher-binding-energy shoulder corresponding to surface-adsorbed species, such as hydroxyl groups or adsorbed water. The dominance of the lattice oxygen peak indicates that most oxygen atoms are integrated within the perovskite structure. At the same time, the minor surface contributions reflect a clean film surface with limited contamination [25].

This comprehensive XPS assessment underscores the chemical integrity and compositional fidelity of the synthesized films, while also providing nuanced insight into the interplay of oxidation states that could influence device performance. Such critical surface analysis is indispensable for correlating the material's surface chemistry with its functional attributes in optoelectronic and catalytic applications.

3.5 UV-Vis Analysis

Figure 7(a) presents the absorbance spectra of $CeTiO_3$ thin films measured over the wavelength range of 300-800 nm, with each spectrum corresponding to a distinct substrate temperature during film deposition. At lower substrate temperatures, the films exhibit comparatively lower absorbance throughout the spectral range, and the absorption edge indicative of the optical band gap appears at a shorter wavelength (higher energy). This suggests the presence of smaller grain sizes, greater disorder, or higher defect density, resulting in less efficient light absorption and a broader distribution of localized states within the band gap. As the substrate temperature increases, a notable enhancement in absorbance is observed, particularly in the ultraviolet and near-visible regions. The absorption edge shifts toward longer wavelengths (lower energies), reflecting a reduction in the optical band gap [26]. This red-shift is commonly attributed to improved crystallinity, grain growth, and reduced structural defects, as higher deposition temperatures facilitate better atomic rearrangement and phase purity. The wavelength-dependent absorbance profiles as a function of substrate temperature clearly demonstrate that optimizing deposition temperature is essential for tailoring the optical properties of $CeTiO_3$ thin films [27].

At lower substrate temperatures (350 °C), the films show higher transmittance across the visible region, with a gradual decline as the wavelength approaches the ultraviolet. The absorption edge, characterized by a sharp drop in transmittance, appears at a shorter wavelength (370 nm), indicating a wider optical band gap and a relatively disordered structure with smaller crystallite sizes. As the substrate temperature increases (400 °C), the transmittance in the visible range decreases, and the absorption edge shifts toward longer wavelengths.

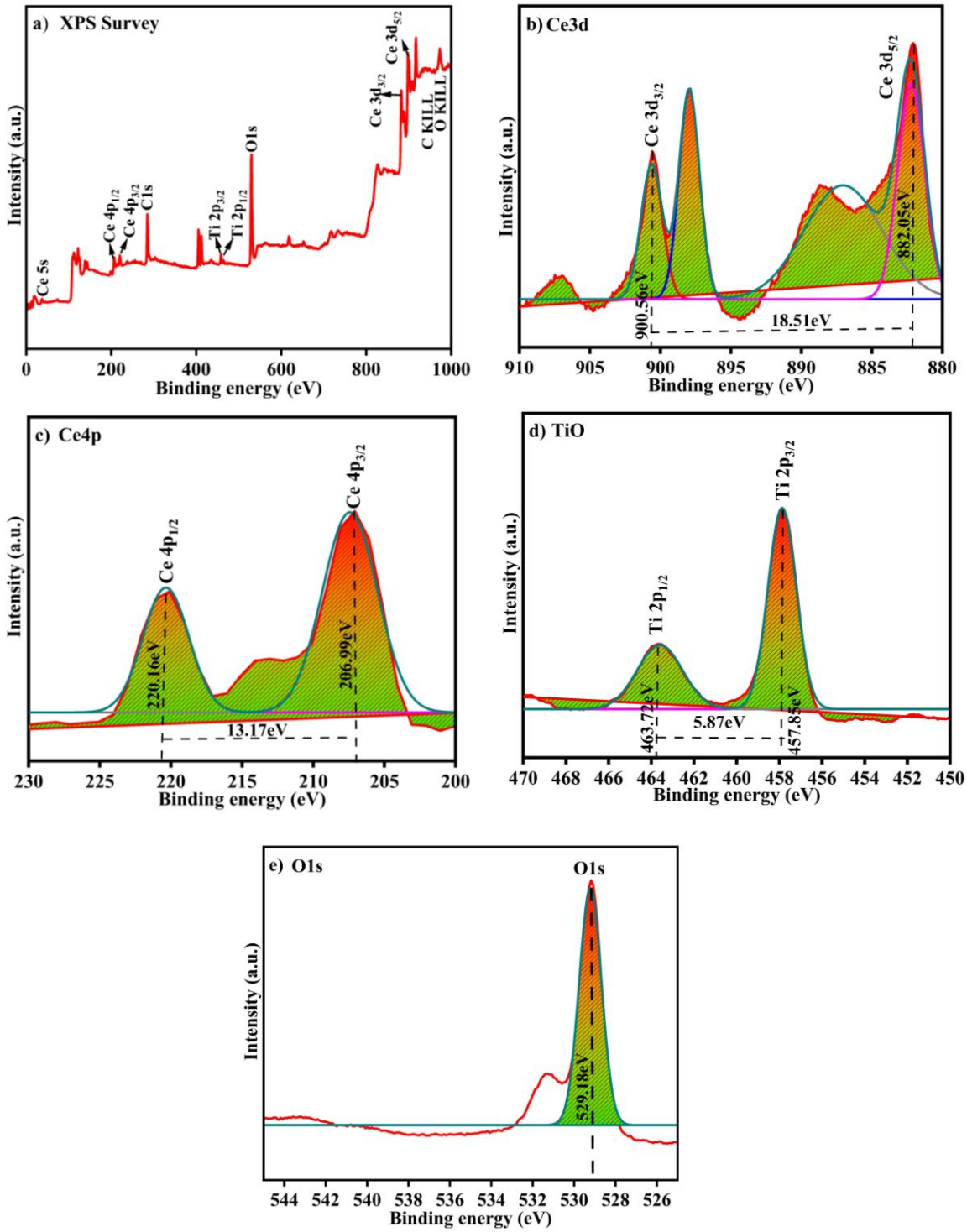

Figure 6 (a-e). XPS Spectra of a spray-deposited $CeTiO_3$ film.

Table 5. The measured XPS region of Ce, Ti, and O

XPS region	Component	Binding energy (eV)	Assignment	Relative area (%)
Ce 3d	Ce3d3/2	900.56 eV	Ce^{4+} component	33.16
Ce 3d	Ce3d5/2	882.05 eV	Ce^{3+} component	66.84
Ti 2p	Ti2p1/2	463.72eV	Ti^{4+}	33.90
Ti 2p	Ti2p3/2	457.85eV	Ti^{4+}	66.10
O 1s	O1s	529.18eV	O^{2-}	100

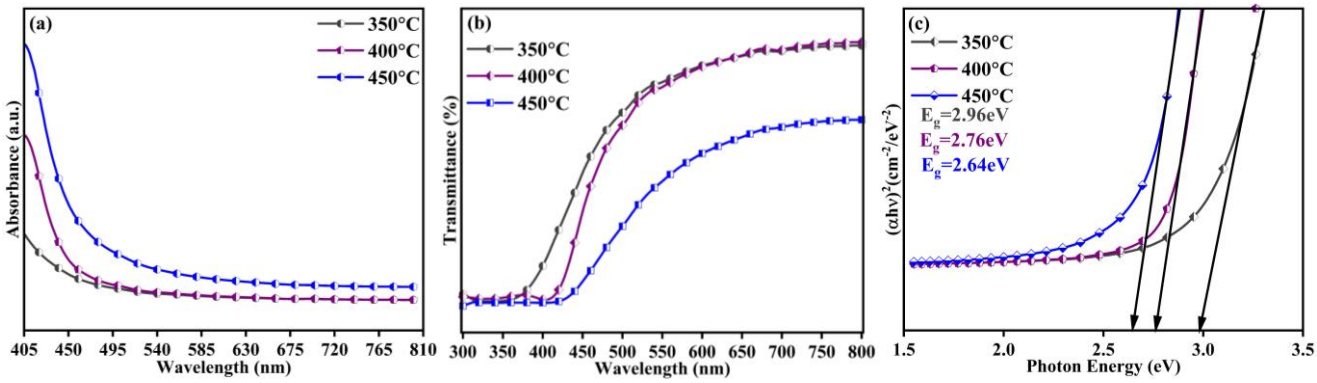

Figure 7(a) Absorbance of $CeTiO_3$ thin films at various temperatures, **(b)** transmittance spectra of $CeTiO_3$ thin films at various temperatures, and **(c)** the dependence of (αhυ) 2 on hυ for $CeTiO^3$ thin films at different temperatures.

Table 6. Optical parameters of spray-coated $CeTiO_3$ thin films

Temperature (ºC)	Adsorption Coefficient (α)×10⁶(cm)⁻¹	Extinction Coefficient (k)	Band gap energy (E_g)eV	Refractive index (n)	Optical Conductivity X σ_{OPT}×10⁹ (Ω -Cm)⁻¹
350	2.871	1.055	2.96	2.786	4.917
400	1.859	6.544	2.76	0.235	2.828
450	1.989	7.050	2.64	0.136	9.901

This redshift in the absorption edge at 395 nm corresponds to a narrower optical band gap, typically associated with enhanced crystallinity, increased grain size, and improved film density. Higher substrate temperatures (450 °C) promote greater atomic mobility during deposition, resulting in films with more compact microstructures and fewer defects. These features enhance the light absorption edge at 430 nm and reduce transmission, especially in the ultraviolet region where the films become increasingly opaque [28].

The overall decrease in visible transmittance with increasing temperature (Figure 7(b)) suggests that optical properties can be finely tuned by adjusting the deposition conditions, enabling optimization for specific applications such as UV-blocking coatings, optoelectronics, or photovoltaics. Careful adjustment of substrate temperature allows for precise tailoring of transparency and absorption characteristics to meet the requirements of targeted device applications.

The observed bandgap narrowing (2.96-2.64 eV) also indicates improved electronic coupling in the lattice and reduced localized trap states, both of which benefit optoelectronic device performance. Such tunability of the optical bandgap via substrate temperature adjustment is particularly advantageous for optimizing $CeTiO_3$ films in applications ranging from photovoltaics to photocatalysis, where precise control over light absorption characteristics is crucial. The data presented in Figure 7(c) and Table 6 confirm that substrate temperature is a key parameter for modulating the optical bandgap of $CeTiO_3$ thin films, enabling fine-tuning of their functional properties for specific technological applications.

3.6 Photoluminescence Spectroscopy

Photoluminescence (PL) emission in $CeTiO_3$ films is generally divided into two main regions: near-band-edge ultraviolet emission and deep-level defect-related visible emission, as shown in Figure 8. UV emission usually results from direct recombination of electrons in the conduction band with holes in the valence band, indicating an intrinsic electronic transition. Instead, visible light arises from photogenerated electrons and their coupling to defect states in $CeTiO_3$ interstitials [29]. These negative states play an essential role in generating the PL spectrum, which shows distinct blue and green colors. The presence of defects in the $CeTiO_3$ lattice is confirmed by blue emission (around 411 nm) and green emission (around 491 nm). The peaks near 361 nm and 376 nm are associated with singly ionized oxygen vacancies, further emphasizing the role of intrinsic and extrinsic defects in the optical properties. NBE UV emissions are attributed to free electron-hole pair transitions and are affected by the film morphology; their intensity is inversely proportional to the crystallite size. This suggests that smaller crystallites increase emission because the surface area/volume ratio increases, promoting radiative recombination [30].

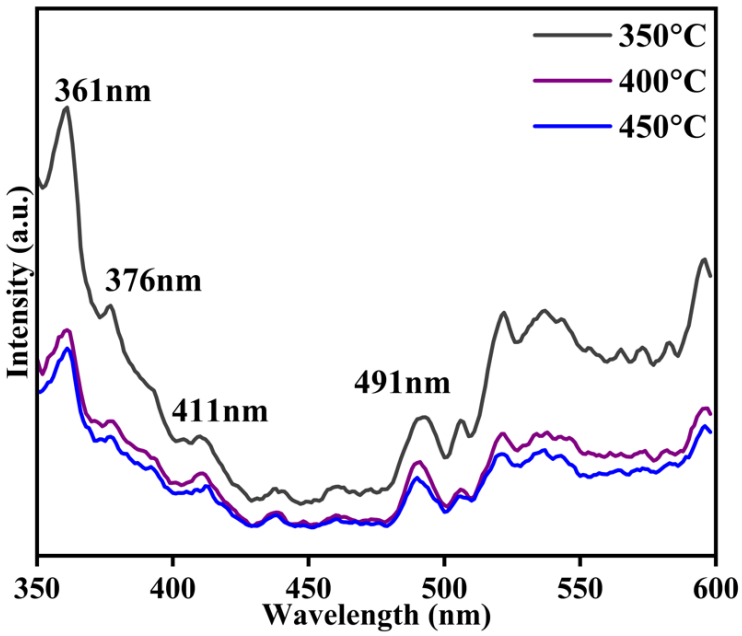

Figure 8. Photoluminescence spectra of $CeTiO_3$ thin films at different temperatures.

This change demonstrates $CeTiO_3$'s ability to absorb visible light at room temperature. The prepared films show strong, broad emission peaks, especially in the visible region, indicating their suitability for optoelectronic devices. The interaction between morphology, defect states, and combination processes determines the luminescence efficiency and provides a way to design optical devices for photodiode applications.

3.7 Electrical property

3.7.1. Electrical Conductivity

The films were tested in two devices, using a Keithley electrometer, to measure DC conductivity. Figure 9 presents the DC conductivity results as current-voltage characteristics. Table 7 lists the DC electrical conductivity parameters of the $CeTiO_3$ thin film for different temperatures. Compute the efficiency [σ_{dc}] and energy efficiency Ea of the film using the equation. These calculations give us an idea of the film's electrical characteristics under electrical load, helping us clearly understand its electrical behavior.

$$\sigma_{dc} = \left(\frac{I}{V}\right) \times \left(\frac{d}{A}\right) \frac{S}{cm} \quad (8)$$

The electrical conductivity of $CeTiO_3$ materials depends on parameters such as output current (I), power dissipation (V), probe density (d), and cross-sectional area (A).

The electrical conductivity of $CeTiO_3$ films ranges from 7.42×10^{-10} S/cm to 5.98×10^{-10} S/cm, mainly due to the material's response to temperature changes. The heating element enables this change, improving the material's ohmic behavior at high temperatures and reducing resistance loss in the PN junction diode [31]. DC conductivity [σdc] is ideal for PN junction diodes where a stable, defect-free path is required. Activation energy Ea (the minimum energy needed to overcome atomic forces) also plays an essential role in transport via thermally activated conduction. This suggests that strong thermal energy drives charge flow [32].

$$Ea = \text{slope value } X\left(\frac{K_B}{e}\right) eV \quad (6)$$

The activation energy decreases with increasing film thickness, further improving device efficiency. These enhancements are attributed to the smooth morphology, reduced crystal defects, and refined optical characteristics of the films [33-35].

3.7.2. Rectification behavior of $CeTiO_3$/p-Si Structure.

The current-voltage (I-V) characteristics in dark and light conditions provide a good idea of the properties of photodiodes and the performance of the PN junction diode. Although this work did not perform direct Hall effect measurements, previous studies have shown that $CeTiO_3$ films deposited under comparable conditions exhibit n-type conductivity [36, 37]. Based on this literature, the $CeTiO_3$/p-Si device is presumed to form a P-N junction; however, this assignment should be regarded as tentative pending direct carrier-type confirmation. Figure 10 illustrates the fabricated CeTiO3/p-Si Photodiode. Figure 11 (a-c) shows the I-V characteristics of $CeTiO_3$/p-Si under illumination. The PN junction diode photocurrent performance was measured using a Keithley electrometer, sweeping from -10 V to +10 V through a negative contact. $CeTiO_3$/p-Si diodes were tested under halogen light.

$$I = Io\,[exp\,(q(V - IRs)/\,nKBT) - 1] \quad (7)$$

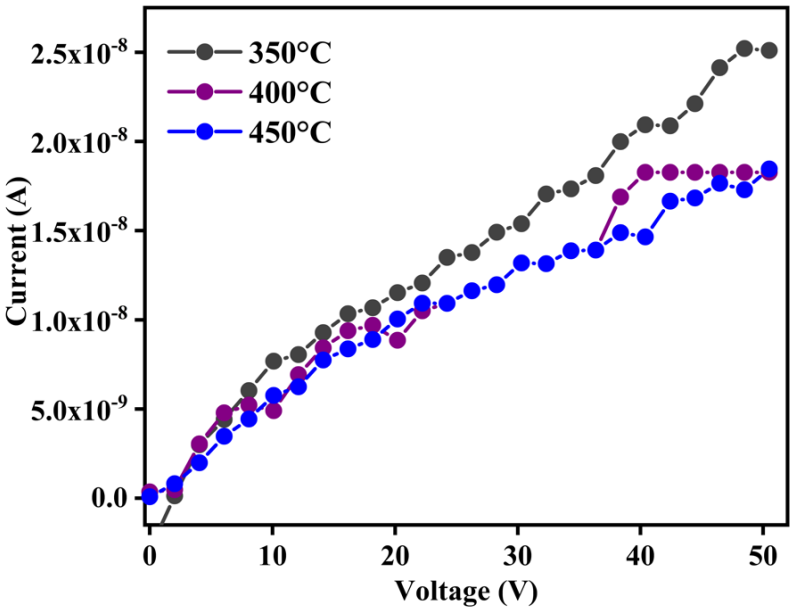

Figure 9. Current vs voltage plot of the thin films using DC electrical conductivity.

Table 7. DC electrical conductivity parameters of $CeTiO_3$ thin film for different temperatures

Temperature (°C)	**Resistivity (ρ)**	**Average Conductivity σ_{dc} (S cm^{-1})**
350	1.66×10^{9}	7.42×10^{-10}
400	1.81×10^{9}	6.36×10^{-10}
450	1.94×10^{9}	5.98×10^{-10}

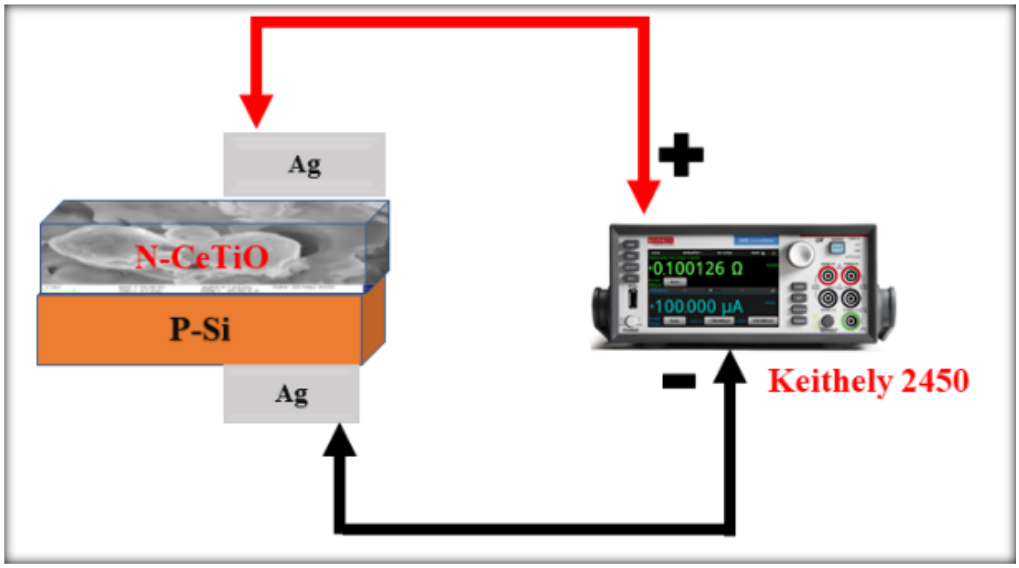

Figure 10. Illustration of fabricated $CeTiO_3$/p-Si Photodiode.

$$Io = AA * T2\ exp\ (-q\phi B/KBT) \quad (8)$$

The parameters affecting the diode performance include saturation current I_0, electron charge q, bias voltage V, ideality factor n, potential barrier height Φ_B, Boltzmann constant K_B, and temperature. Table 8 shows the optimized parameters used for device fabrication. The optimum value of n is determined by analyzing the measured voltage V.

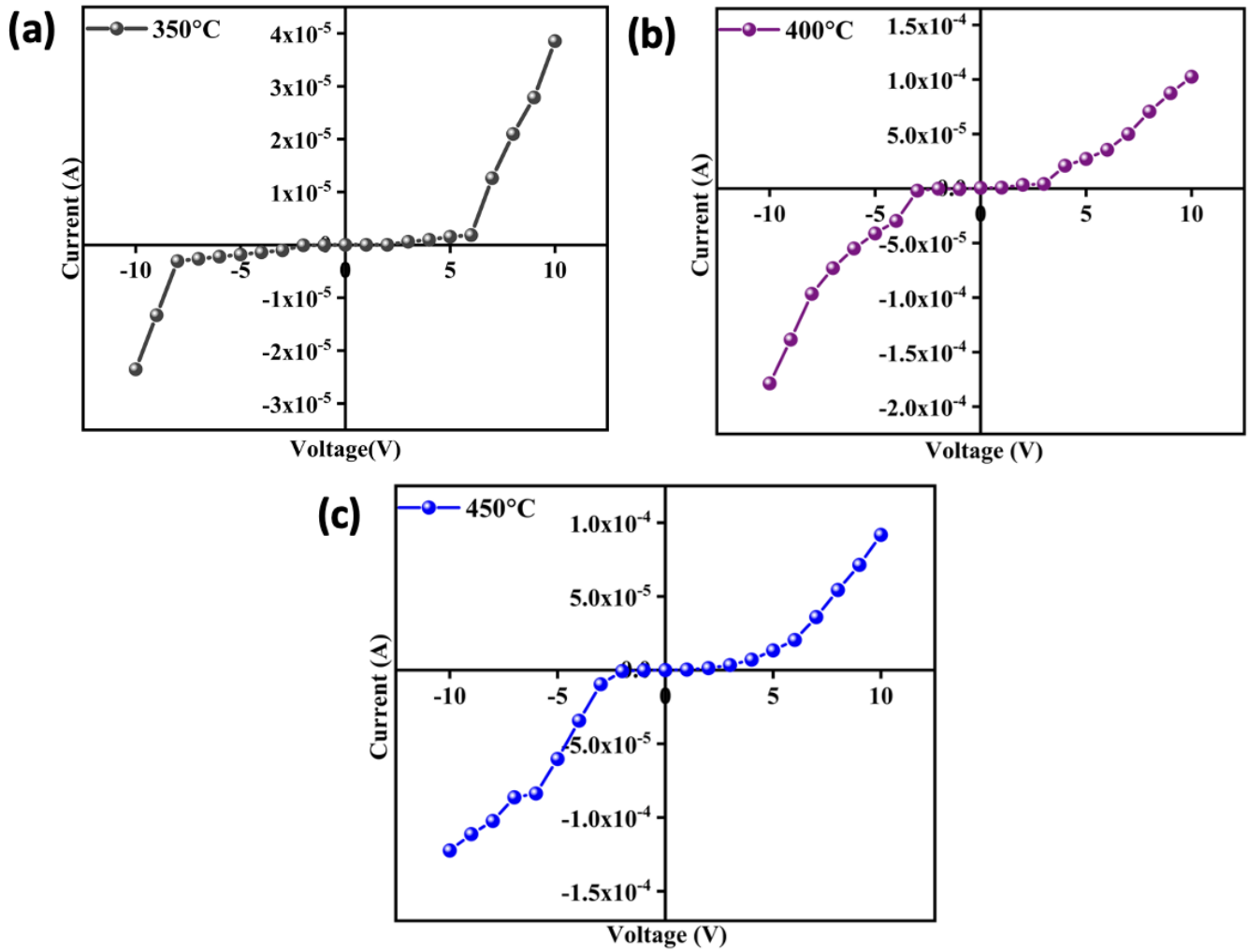

Figure 11. Rectification behavior of the $CeTiO_3$/p-Si photodiode

Table 8. Optimized parameters used for device fabrication

Parameter	**value**
p-Si orientation	(100)
Resistivity	1–10 Ω·cm
Doping concentration	~10^{15}–10^{16} cm^{-3}
Wafer thickness	725 µm
Exposed junction area	1 cm^2
Native-oxide removal	Dilute HF treatment
Ag deposition method	Doctor blade method
Top Ag contact area	0.11 cm^2
Ag thickness	40 nm
Backside Ag contact	0.11 cm^2
Post-metallization treatment	Not necessary

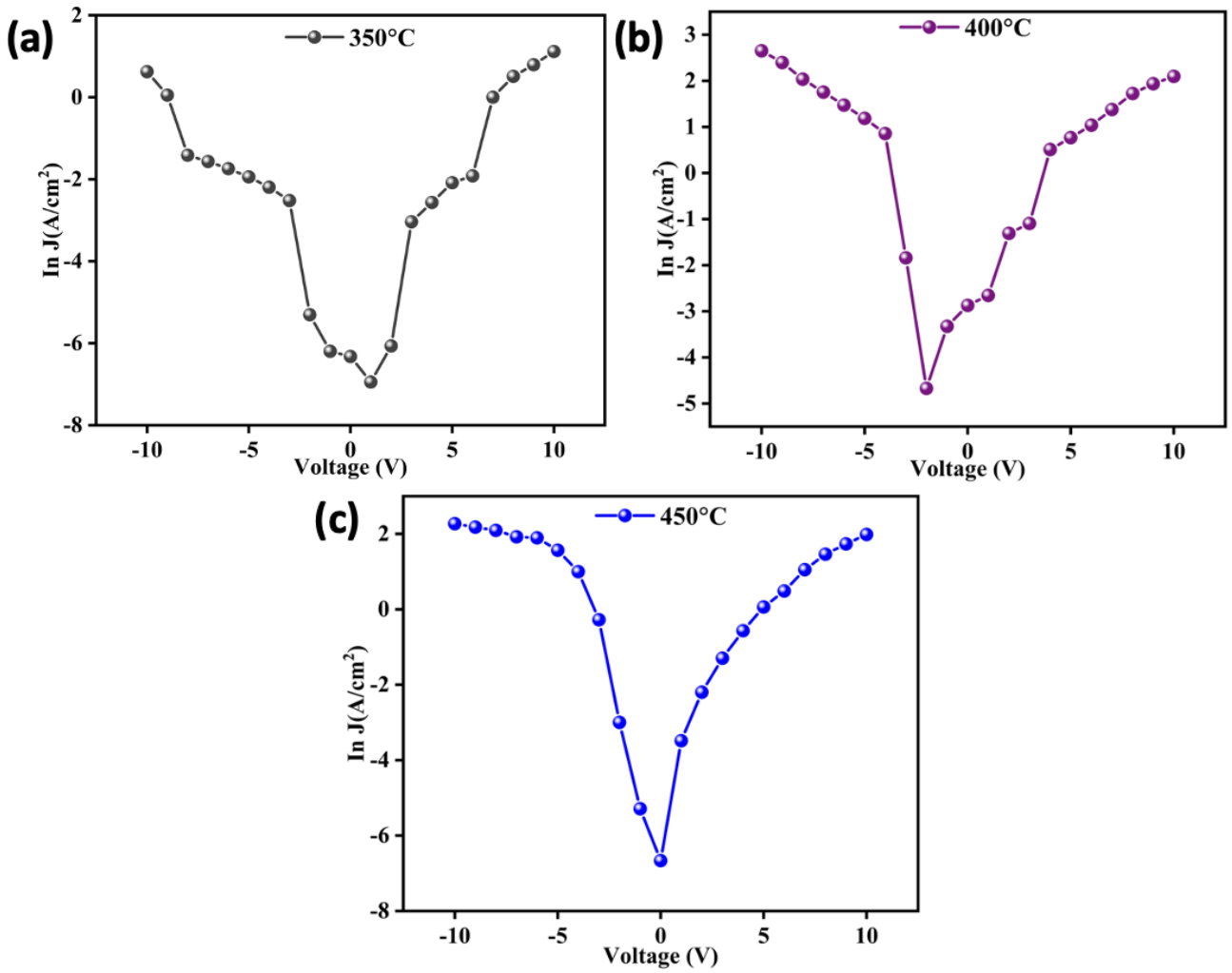

Figure 12. The forward and reverse-bias ln(J)-V characteristics of the $CeTiO_3$ /p-Si Photodiode.

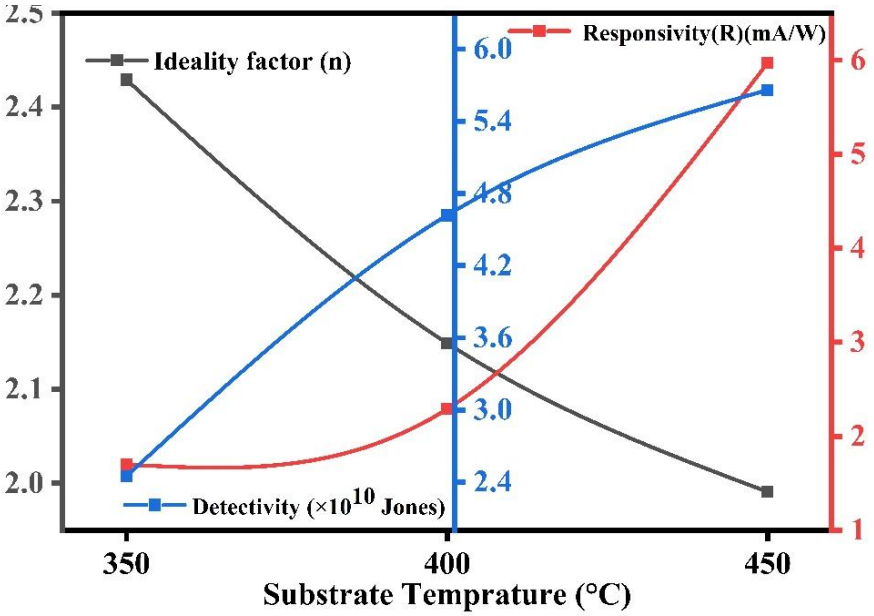

Figure 13. Photodiode properties of the pure $CeTiO_3$ /p-Si Photodiode.

Table 9. Barrier height (ΦB), Ideality factor (n), Responsivity (R)(mA/W), Quantum Efficiency (%), Detectivity (×10^{10}Jones) of the $CeTiO_3$/p-si diode with different temperature

Temperature (ºC)	Ideality Factor (n)	Barrier Height (ΦB)	Responsivity (R)(mA/W)	Quantum Efficiency (%)	Detectivity (×10^{10}Jones)
350	2.429	0.396	1.70	2.32	2.45
400	2.149	0.401	2.29	6.60	4.62
450	1.991	0.411	5.97	8.89	5.66

Table 10. Comparative analysis of various characterization parameters of $CeTiO_3$ thin films for different temperatures

Parameter	350°C	400°C	450°C
Crystallite Size (nm)	11.4	12.3	12.9
Micro strain	0.1592	0.1621	0.1636
Dislocation density	7.6091	6.5794	5.9377
Optical band gap (eV)	2.96	2.76	2.64
Average Particle size (nm)	17.42	24.97	34.97
Conductivity (S/cm)	7.42×10^{-10}	6.36×10^{-10}	5.98×10^{-10}
Ideality factor	2.429	2.149	1.991
Barrier height (eV)	0.396	0.401	0.411

Figure 12(a-c) shows the forward- and reverse-bias ln(J)-V characteristics of a pure $CeTiO_3$/p-Si PN junction diode. Interestingly, various research groups working with different instruments and deposition methods have reported similar behavior [38, 39]. The diode efficiency is strongly affected by the ideality factor n and barrier height ΦB, which positively and significantly affect device operation.

$$\text{Ideality factor (n)} = \frac{q}{K_B T}\frac{dV}{d(\ln I)} \quad (9)$$

$$\text{Barrier height } (\phi_B) = \frac{K_B}{q}\ln\left(\frac{AA^*T^2}{I_0}\right) \quad (10)$$

The target value (n) of PN junction diodes varies from 2.429 to 1.991, deviating from the shared values. When n = 1, the diode operates under ideal thermionic emission conditions; however, the commonality is more valuable. The observed ideality factors (n ≈ 2 or greater) suggest that current transport is not governed solely by ideal thermionic emission. Possible contributions from interface-state-assisted recombination, series resistance, and leakage currents were considered. Additionally, interface states at the $CeTiO_3$/p-Si interface may facilitate recombination, further increasing n. These findings indicate that the dominant conduction mechanism likely involves a combination of thermionic emission, recombination, and parasitic resistance effects [40, 41]. The $CeTiO_3$/p-Si diode exhibits excellent brightness under illumination, with I-V characteristics of n = 1.99 and Φ_B = 0.41 eV. Boundary defects can block carriers but facilitate transport by providing alternative paths [42-45]. Figure 13 shows the photodiode properties of the pure CeTiO3 /p-Si Photodiode. The photodiode parameters (Table 9) improve markedly as a direct consequence of advances in film structure, morphology, chemical composition, and optical absorption. High-quality films, as evidenced by sharp XRD peaks, uniform SEM morphology, well-defined XPS spectra, and steep UV-Vis absorption edges, consistently yield photodiodes with lower ideality factors, higher barrier heights, superior detectivity, and greater responsivity. This correlation confirms (Table 10) that careful optimization of substrate temperature and deposition protocols is essential to realize the full potential of $CeTiO_3$-based photodiodes in advanced optoelectronic applications.

4. Conclusion

This study comprehensively elucidates how substrate temperature affects the structural, optical, and electronic properties of $CeTiO_3$ thin films, with direct implications for photodiode device performance. Increasing the substrate temperature from 350°C to 450°C yields a series of favorable changes across all

measured parameters, underscoring a pivotal role in thin-film fabrication.

Structurally, XRD and SEM analyses show that higher substrate temperatures improve crystallinity and grain growth, as evidenced by increases in both crystallite and average particle sizes. The concurrent reduction in dislocation density and only marginal increase in microstrain point to enhanced lattice ordering with minimal introduction of strain-induced defects. These microstructural refinements help minimize grain-boundary scattering and promote more efficient charge-carrier pathways.

Optically, UV-Vis spectroscopy shows a consistent narrowing of the optical band gap with increasing deposition temperature. This red-shift, from 2.96 eV to 2.64 eV, reflects enhanced structural order and reduced quantum confinement effects, as well as suppression of localized defect states that typically broaden the band gap in less-ordered films. This band-gap engineering maximizes light absorption in the visible spectrum, improving the material's photonic response.

The ideality factor approaches unity as substrate temperature increases, indicating a transition toward more ideal diode characteristics and reduced non-radiative recombination. The gradual increase in barrier height further attests to the formation of cleaner, more effective junctions, which are essential for suppressing leakage currents and enhancing rectification behavior. Together, these changes enhance the photodiode's rectification behavior, photoresponse, and operational stability. Higher substrate temperatures produce devices that are not only more efficient in photon-to-electron conversion but also exhibit lower dark currents and improved sensitivity.

In summary, substrate temperature emerges as a critical lever for tailoring the multifunctional performance of $CeTiO_3$ thin films. These findings provide a valuable framework for designing and engineering high-performance oxide-based photodetectors and other optoelectronic devices.

References

[1] J.M. Shah, Y.L. Li, Th Gessmann, E. Fred Schubert. Experimental analysis and theoretical model for anomalously high ideality factors (n≫ 2.0) in AlGaN/GaN pn junction diodes. Journal of Applied Physics, 94, (2003) 2627-2630. https://doi.org/10.1063/1.1593218

[2] H. Ohta, N. Kaneda, F. Horikiri, Y. Narita, T. Yoshida, T. Mishima, T. Nakamura, Vertical GaN pn junction diodes with high breakdown voltages over 4 kV. IEEE Electron Device Letters 36(11), (2015) 1180-1182. https://doi.org/10.1109/LED.2015.2478907

[3] M. Vidhya, N. Sumathi, K. Sadaiyandi, P. Rajapandi, K. Elumalai, S. Arunkumar, A. Nancy Mary, R. Marnadu, Farhat S. Khan, M. Shkir. Effect of molar concentration on optoelectronic properties of NiO nanoparticles for pn junction diode application. Sensors and Actuators A: Physical, 366, (2024) 114995. https://doi.org/10.1016/j.sna.2023.114995

[4] H.M. Elmehdi, K. Ramachandran, S. Chidambaram, G.T. Mani, S. Pandiaraj, S.A. Alqarni, K. Daoudi, M. Gaidi. Diode characteristics, piezo-photocatalytic antibiotic degradation and hydrogen production of Ce^{3+} doped ZnO nanostructures. Chemosphere, 350, (2024) 141015. https://doi.org/10.1016/j.chemosphere.2023.141015

[5] A. K. Hassan, and Ghusoon M. Ali. Thin film NiO/$BaTiO_3$/ZnO heterojunction diode-based UVC photodetectors. Superlattices and Microstructures 147, (2020) 106690. https://doi.org/10.1016/j.spmi.2020.106690

[6] T.A.M. Taha, A.H. Alshammari, M.M.S. Sanad, S.S. Elsherif, M.S. Eraky, A.M. Alenad, K.S. El-Nasser, H.H. Hamdeh, Impact of Ca^{2+}, Ce^{3+} codoping on $ZnSnO_3$-SnO_2 heterostructure for dielectric, optoelectronic and solar cell applications. Journal of Electroanalytical Chemistry 952, (2024) 117955. https://doi.org/10.1016/j.jelechem.2023.117955

[7] S. Kumar, R. Singh, R. Tiwari, N. Gupta, S. Sharma, Recent advances in biofuel production and the application of nanotechnology for environmental sustainability: A comprehensive review. Renewable and Sustainable Energy Reviews, 182, (2023) 113456. https://doi.org/10.1016/j.rser.2023.113456

[8] N. Dey, S. Vickram, S. Thanigaivel, S. Manikandan, R. Subbaiya, N. Karmegam, W. Kim, M. Govarthanan. Aftermath of nanomaterials on lipid profile of microalgae as a radical fuel supplement–A review. Fuel, 333, (2023) 126444. https://doi.org/10.1016/j.fuel.2022.126444

[9] A.S. Vickram, H.A. Samad, S.K. Latheef, S. Chakraborty, K. Dhama, T.B. Sridharan, T. Sundaram, G. Gulothungan. Human prostasomes and extracellular vesicle Biomarkers for male infertility and prostate cancer: The journey from identification to current knowledge. International journal of biological macromolecules, 146, (2020) 946-958. https://doi.org/10.1016/j.ijbiomac.2019.09.218

[10] S. Thanigaivel, S. Vickram, N. Dey, P. Jeyanthi, R. Subbaiya, W. Kim, M. Govarthanan, N. Karmegam. Ecological disturbances and abundance of anthropogenic pollutants in the aquatic ecosystem: Critical review of impact assessment on the aquatic animals. Chemosphere 313, (2023) 137475. https://doi.org/10.1016/j.chemosphere.2022.137

475

[11] S. Mahapatra, A.S. Vickram, T.B. Sridharan, R. Parameswari, M.R. Pathy, Screening, production, optimization, and characterization of β-glucosidase using microbes from shellfish waste. 3 Biotech, (2016) 1-10. https://doi.org/10.1007/s13205-016-0530-7

[12] J. Zhang, Y. Liu, L. Wang, H. Li, Z. Chen, Facile synthesis of CeO2-based nanocomposites as efficient catalysts for organic pollutant degradation and oxygen evolution reaction. Journal of Environmental Chemical Engineering, 11, (2023) 110123. https://doi.org/10.1016/j.jece.2023.110123

[13] M. Li, X. Zhao, H. Wu, J. Sun, L. Yang, Highly active CeO2-based hybrid nanomaterials as bifunctional electrocatalysts for enhanced oxygen evolution reaction. Electrochimica Acta, 451, (2023) 142542. https://doi.org/10.1016/j.electacta.2023.142542

[14] F. Mukhtar, T. Munawar, K.M. Batoo, H. Khursheed, M.S. Nadeem, S. Hussain, J. Ponraj, M. Koc, F. Iqbal, Oxygen vacancies generation in CeO2 via Y/Nd co-doping with accelerated charge separation by decorating on rGO sheets for sunlight-driven photodegradation of hazardous dyes. Ceramics International, 50(7), (2024) 11486-11499. https://doi.org/10.1016/j.ceramint.2024.01.049

[15] F. Nasim, H. Ali, A. Waseem, M.A. Nadeem, Investigating the effect of CeO_2 on the radical scavenging activity of Pt@CoOx/NC@CeO_2 during the electrocatalytic oxygen reduction reaction in acidic and alkaline environments. Materials Advances, 5, (2024) 2545-2555. https://doi.org/10.1039/d4ma00041b

[16] K. Mohanraj, D. Balasubramanian, J. Chandrasekaran, A. Chandra Bose. Synthesis and characterization of Ag-doped CdO nanoparticles for PN junction diode application. Materials Science in Semiconductor Processing, 79, (2018) 74-91. https://doi.org/10.1016/j.mssp.2018.02.006

[17] N. Sumathi, A. Clara Dhanemozhi, D. Thangaraju, Saheed A. Adewinbi, K. Mohanraj, R. Marnadu, M. Shkir, Hydrothermal synthesis of self-assembled potassium-doped Graphene semiconducting nanoparticles for p-Si/n-Graphene junction diode applications. Surfaces and Interfaces, 26, (2021) 101408. https://doi.org/10.1016/j.surfin.2021.101408

[18] H. Waheed, K. Javaid, A. Ali, K. Mahmood, M. Imran Arshad, N. Amin, M. Amami, S.A. Aldulmani, Z. Mustafa, U. Shehzad, R. Anjum, H. Anwar, A. Bibi, Z. Afzal, Z. Rasheed, M. Saleem, M.Y. Ali, Band alignment engineering of p-Ge/n-Si heterojunction for low-cost tandem solar cell applications. Optical Materials, 157, (2024) 116222. https://doi.org/10.1016/j.optmat.2024.116222

[19] M. Justin Paul, R. Suresh, T. Akila, V. Balasubramani, S. Muthusamy, S. Alarifi, R. Ayub. Standardizing the optimal photodiode performance of CuO nanostructures through various morphological patterns. Journal of Alloys and Compounds, 1000, (2024) 175092. https://doi.org/10.1016/j.jallcom.2024.175092

[20] P. Vidhya, K. Shanmugasundaram, T. Sasikala, T. Akila, V. Balasubramani, A.T. Rajamanikam, N.A. Siddiqui, A. Khan, Optimization of PN Junction Diodes Using Crack-Free PbS Thin Films: The Role of Y^{3+} Doping via Jet Nebulizer Spray Pyrolysis. Physica B: Condensed Matter, 699, (2024) 416836. https://doi.org/10.1016/j.physb.2024.416836

[21] E. Hannachi, M. I. Sayyed, K.A. Mahmoud, Y. Slimani, S. Akhtar, Badriah Albarzan, A.H. Almuqrin, Impact of tin oxide on the structural features and radiation shielding response of some ABO_3 perovskite ceramics (A= Ca, Sr, Ba; B= Ti). Applied Physics A, 127, (2021) 970. https://doi.org/10.1007/s00339-021-05092-6

[22] K.A. Qurbani, O. Amiri, G.M. Othman, A.A. Fatah, N.J. Yunis, M. Joshaghani, S.S. Ahmed, N.A. Abdulrahman, Enhanced antibacterial efficacy through piezo-memorial effect of $CaTiO_3/TiO_2$ Nano-Composite. Inorganic Chemistry Communications, 165, (2024) 112470. https://doi.org/10.1016/j.inoche.2024.112470

[23] A. Kramar, Y. Bibik, A. Dyachenko, O. Chernyayeva, V. Vorobets, G. Kolbasov, N. Smirnova, S. Gaidai, O. Ischenko, A. Eremenko, O. Linnik , Advanced design of sol-gel derived multilayered cerium titanate films: structural, surface, photo electrochemical and photocatalytic properties. Materials Chemistry and Physics, 324, (2024) 129679. https://doi.org/10.1016/j.matchemphys.2024.129679

[24] Q. Zhang, R. Cui, J. Wu, Z. Tang, Exploring the Influence of CeTiO x Morphology on Wet Catalytic Oxidation Performance of Phenol over the Ru-Based Catalyst. Industrial & Engineering Chemistry Research, 63(40), (2024) 17014-17024. https://doi.org/10.1021/acs.iecr.4c01515

[25] N.F. Nazari, M. Rajabi, A.Z. Moshfegh, UV-activated heterojunction in $BaTiO_3$ decorated ZnO nanorods for faster and more efficient photodetector. Sensors and Actuators A: Physical 379, (2024) 115877. https://doi.org/10.1016/j.sna.2024.115877

[26] S. Sha, K. Tang, M. Liu, P. Wan, Z. Liu, D.N. Shi, C. Kan, M. Jiang, F. Pyro-Phototronic, Effect Enhanced Self-Powered UV Photodetectors Based on $BaTiO_3$@ MXene/4H-SiC Heterojunction. ACS Photonics, 11, (2024) 4472-4485. https://doi.org/10.1021/acsphotonics.4c01573

[27] M. Chen, H. Ding, Y. Wang, Q. Hou, X. Hu, J. Deng, W. Sun, Multilayered BCST/PZT thin films on GaN substrate for ultraviolet photodetector applications. Journal of Alloys and Compounds, 988, (2024) 174159. https://doi.org/10.1016/j.jallcom.2024.174159

[28] Z. Bi, Y. Zhang, Y. Zhang, X. Liu, Y. Ma, X. Li, C. Liu, Y. Chen, J. Zhou, S. Ruan, MSM UV photodetector with low dark current based on GaInO/$SrTiO_3$ heterojunction, Materials Science in Semiconductor Processing, 170, (2024) 107973. https://doi.org/10.1016/j.mssp.2023.107973

[29] B. Chen, J.W. He, Y.J. Wang, Driving magnetic oscillation by electric flip in Permalloy/$BaTiO_3$ composite. Results in Physics, 58, (2024) 107542. https://doi.org/10.1016/j.rinp.2024.107542

[30] Y. Liu, D. Zhao, X. Sun, F. Cui, S. Zhang, X. Shang, Z. Xuan, J. Xiao, J. Wang, Y. Ren, Flexible Cu_2O/Cu film self-powered photodetector for high visible light selection and fast response. Current Applied Physics, 58, (2024) 44-50. https://doi.org/10.1016/j.cap.2023.12.002

[31] Y. Atheeswaran, R. Suresh, M.A. Manthrammel, M. Shkir, E.H. Ibrahim, T. Subramani, Conversion of complex molecules into useful small compounds via photocatalytic decolorization using $SrTiO_3$ thin films. Journal of Materials Science: Materials in Electronics, 37, (2026) 516. https://doi.org/10.1007/s10854-026-16903-y

[32] T.G. Vignesh Prabhu, J. Chandrasekaran, V. Balasubramani, P. Vivek, A. Yogeshwaran, M. Manigandan, Amal M. Al-Mohaimeed, Wedad A. Al-Onazi. Natural dye-sensitive solar cells (N-DSSCs) are fabricated using TiO2/1 wt% SrTiO3 as photoanodes. Optical Materials 148, (2024) 114973. https://doi.org/10.1016/j.optmat.2024.114973

[33] A. Gupta, S. Kumar, R. Singh, Structural, optical and electrical properties of CeO_2 nanostructures synthesized via a facile hydrothermal method. Materials Science in Semiconductor Processing, 163, (2024) 107691. https://doi.org/10.1016/j.mssp.2024.107691

[34] N. Anttu, E.M. Fiordaliso, J.C. Garcia, G. Vescovi, D. Lindgren, Analysis of Nanowire pn-Junction with Combined Current–Voltage, Electron-Beam-Induced Current, Cathodoluminescence, and Electron Holography Characterization. Micromachines, 15, (2024) 157. https://doi.org/10.3390/mi15010157

[35] Y. Lv, S. Xie, J. Huang, S. Lu, D. Luo, Y. Xiang, Bio-p–n Junction–Derived Bio–Diodes with Opto-Ionotronic Switching and Rectification Effects. Advanced Functional Materials, 34(46), (2024) 2407744. https://doi.org/10.1002/adfm.202407744

[36] W. Liu, Y. Zhang, X. Li, J. Wang, Electrical and optical properties of $CeTiO_3$ ceramics: Evidence of n-type conductivity by Hall effect measurements. Journal of Alloys and Compounds, 924, (2022) 166522. https://doi.org/10.1016/j.jallcom.2022.166522

[37] E. Maskar, A. Fakhim Lamrani, A. Es-Smairi, A. Louradi, A. Yvaz, D.P. Rai, Electronic, magnetic, and thermodynamic properties of orthorhombic $CeScO_3$, $CeTiO_3$, and $CeVO_3$ using GGA and GGA+U. Computational Condensed Matter, 38, (2024) e00873. https://doi.org/10.1016/j.cocom.2023.e00873

[38] C. Ma, W. Chen, T. Liu, W. Zhang, B. Zhang, Recent developments in superjunction power devices. Journal of Semiconductors, 45, (2024) 111301. https://doi.org/10.1088/1674-4926/24050003

[39] J. Liu, R. Zhang, M. Xiao, SPidaparthi, Hao Cui, Andrew Edwards, Lek Baubutr, Cliff Drowley, and Yuhao Zhang. "Surge current and avalanche ruggedness of 1.2-kV vertical GaN pn diodes. IEEE Transactions on Power Electronics, 36, (2021) 10959-10964. https://doi.org/10.1109/TPEL.2021.3067019

[40] V. Gopal, Origin of the Shunt Currents and Their Influence on the Ideality Factor (η) of a pn Junction. Journal of Electrical and Electronic Engineering, 10, (2022) 180-183.

[41] V. Balasubramani, T. Akila, R. Suresh, Abdullah N. Alodhay, M. Muthuramamoorthy, K. Sasikumar, Optimizing oxygen vacancy concentrations in CeO_2 thin films for enhanced photodetector sensitivity, Optical Materials, 159, (2025) 116625. https://doi.org/10.1016/j.optmat.2024.116625

[42] M. Li, D. Jiang, M. Zhao. Cu_2O/Ga_2O_3 pn-junction photodetector with low dark current and high detectivity. Journal of Materials Chemistry C, 13, (2025) 718-723. https://doi.org/10.1039/d4tc04165h

[43] A. Biswas, R. Sk, A. Patra, A. Layek, P.P. Ray. Recognition of light-sensing pn junction for hetero-structure $CuInSe_2/TiO_2$ and $CuInSe_2$/HF-TiO_2: Study of carrier transport mechanism. Materials Letters, 379, (2025) 137662. https://doi.org/10.1016/j.matlet.2024.137662

[44] A. Bar, S. Sadhukhan, S. Naskar, Interfacing MCP4921 DAC with Arduino UNO to Characterize a Zener Diode. The Physics Teacher, 63, (2025) 60-63. https://doi.org/10.1119/5.0166940

[45] S.O. Abdellatif, Ahmed A. Ghanem, Ahmat Abdel Wahid, Amr Hatem, and Belal Ahmed. Integration of artificial intelligence with a customized Four-Probe station for IV characteristic classification and prediction. Measurement, 241, (2025)

115676.
https://doi.org/10.1016/j.measurement.2024.115676

Authors Contribution Statement

A. Yogeshwaran: Conceptualization, methodology, investigation, data curation, and writing – original draft. A. Paramesvaran: Writing – review and editing. R. Suresh: Conceptualization, methodology, supervision, investigation, data curation, and writing – original draft. All authors have read and approved the final version of the manuscript.

Funding

The authors declare that no funds, grants, or any other support were received during the preparation of this manuscript.

Competing Interests

The authors declare that there are no conflicts of interest regarding the publication of this manuscript.

Data Availability

The data supporting the findings of this study can be obtained from the corresponding author upon reasonable request.

Has this article been screened for similarity?

Yes